

# The structure of spiral galaxies - II. Near-infrared properties of spiral arms

M.S. Seigar & P.A. James

*Astrophysics Group, Liverpool John Moores University, Byrom Street,  
Liverpool, L3 3AF, U.K.*

*email: mss & paj @staru1.livjm.ac.uk*

11 November 2021

## ABSTRACT

We have imaged a sample of 45 face-on spiral galaxies in the K-band, to determine the morphology of the old stellar population, which dominates the mass in the disk. The K-band images of the spiral galaxies have been used to calculate different characteristics of the underlying density perturbation such as arm strengths, profiles and cross-sections, and spiral pitch angles. Contrary to expectations, no correlation was found between arm pitch angle and Hubble type, and combined with previous results this leads us to conclude that the morphology of the old stellar population bears little resemblance to the optical morphology used to classify galaxies.

The arm properties of our galaxies seem inconsistent with predictions from the simplest density wave theories, and some observations, such as variations in pitch angle within galaxies, seem hard to reconcile even with more complex modal theories. Bars have no detectable effect on arm strengths for the present sample.

We have also obtained B-band images of three of the galaxies. For these galaxies we have measured arm cross-sections and strengths, to investigate the effects of disk density perturbations on star formation in spiral disks. We find that B-band arms lead K-band arms and are narrower than K-band arms, apparently supporting predictions made by the large scale shock scenario, although the effects of dust on B-band images may contribute towards these results.

**Key words:** galaxies: spiral - galaxies: structure - galaxies: fundamental parameters

## 1 INTRODUCTION

Ever since the pioneering work of Lin & Shu (1964, 1966) many theoretical models have been proposed to explain the existence of spiral structure in disk galaxies. Many are based upon the Lin-Shu Hypothesis (e.g. Lin, Yuan & Shu 1969; Roberts 1969; Roberts, Roberts & Shu 1975) which describes spiral patterns as density waves, which cause compression of the gas component as it flows through the arms leading to subsequent star formation. Modal theories (Bertin et al. 1989a, 1989b; Bertin & Lin 1996) are more complex density wave models, which describe disks of galaxies as resonant cavities within which density waves of different modes can co-exist and interfere to produce a range of observed phenomena. Tidal models (Toomre & Toomre 1972; Kormendy & Norman 1979) set up spiral structure through transient density waves, which are caused by the tidal field of a nearby neighbour. Bars can also potentially drive spiral structure (Sanders & Huntley 1976). In this case the formation of arms is driven by the effect of the bar potential on the dissipative

interstellar medium. Finally Stochastic Self-propagating Star Formation (SSPSF) can describe flocculent structure. Here, short irregular arms are produced due to shearing of a part of the disk that has recently formed stars (Gerola & Seiden 1978). SSPSF alone cannot describe Grand-Design structure, but some models (e.g. Sleath & Alexander 1995, 1996) use SSPSF with a weak imposed density wave to describe such global spiral modes.

Many of the recent advances in this area have arisen from a study of the atomic and molecular gas component in spiral galaxies, through studies of HI and CO line emission. This has permitted the detailed mapping of both the distribution and velocity field of the gas in the spiral arms of nearby galaxies, e.g. M81 (Visser 1980) M51 (Tilanus & Allen 1991, 1993; Rand 1993; Nakai et al. 1994), M100 (Knapen 1993; Rand 1995), NGC 3627 (Reuter et al. 1996) and NGC 6946 (Regan & Vogel 1995). These studies find streaming velocities of gas through the spiral arms of order a few 10s of  $\text{km s}^{-1}$ , and also find offsets between the peaks of the gas density and the old stellar population in

the arms and the star formation as revealed by H $\alpha$  emission. All of these findings are in general agreement with the predictions of density wave theories, with the gas being compressed and shocked as it flows into the spiral arm, and subsequently forming stars downstream from the density peak of the spiral arm. However, these studies are only possible in the strongest arms of the nearest spiral galaxies, and hence yield little information on the global importance of density waves in the general population of disk galaxies. Here we undertake the complementary approach of calculating the strength of density waves as mapped out by the old stellar population of a large sample of galaxies, using near-IR K-band ( $2.2\mu\text{m}$ ) imaging. In this waveband the old stellar population is observed (Rix & Rieke 1993), making this the best observational tracer of the stellar mass distribution. Also, K-band measurements are less affected by extinction than measurements in the optical.

In a previous paper (Seigar & James 1998 - hereafter Paper I) we described the properties of the bulges, disks and bars of a sample of 45 galaxies. In this paper we describe how spiral arm structures can be extracted for these galaxies and determine quantitative parameters for them. In section 2 we describe the observations; section 3 describes the data reduction and extraction of all of the spiral arm parameters used in the analysis; section 4 then draws on these parameters in discussing, in turn, each of the theoretical models of spiral structure; in section 5 we describe tests of models of star formation in spiral galaxy disks and in section 6 we summarise our findings.

## 2 OBSERVATIONS

A sample of 45 face-on spiral galaxies, selected using the NASA/IPAC Extragalactic Database (NED)<sup>\*</sup>, was observed using the infrared camera IRCAM3 on the United Kingdom Infrared Telescope (UKIRT). IRCAM3 utilises a 256x256 array with a pixel size of 0.286 arcsec, and the observations presented here were made in the J and K bands. The observing dates were 1995 February 5 & 6, 1995 November 18, 19 & 20 and 1996 March 22 & 23. Each galaxy was observed for a total integration time of 1800 seconds in the K-band, and 540 seconds in the J-band. All measurements presented here are taken from the K band images unless otherwise stated. For flat-fielding purposes, sky frames were obtained using equal integration times on areas of nearby blank sky. A dark frame with the same on-chip exposure time was taken both for the galaxy frames and the sky frames. Standard stars, taken from the UKIRT faint standards list, were observed throughout all nights to provide photometric calibration.

This sample spans a range of Hubble types classified as Sa to Sd, including barred and non-barred galaxies as from the Third Reference Catalogue of Bright Galaxy (de Vaucouleurs et al 1991; hereafter RC3). The details of the sample are explained in paper I. The Hubble types of the galaxies are listed in column 2 of table 1.

<sup>\*</sup> The NASA/IPAC Extragalactic Database (NED) is operated by the Jet Propulsion Laboratory, California Institute of Technology, under contract with the National Aeronautics and Space Administration.

## 3 EXTRACTION OF SPIRAL ARM STRUCTURES

In this section we describe the technical details of the extraction of quantitative descriptors of spiral structure in the 45 spiral galaxies. These parameters will then be used in subsequent sections to test theories of spiral structure.

### 3.1 Ellipse Fitting

The RGASP package was used to fit ellipses to the isophotes in the reduced galaxy images. The ellipticity of the outermost ellipses was then adopted and the PROF routine, which takes medians around ellipses at increasing radii, was run keeping this ellipticity and position angle constant. The REBUILD facility in RGASP enables a simulated galaxy to be made up using the ellipticity and position angle and the median surface brightness calculated around these ellipses, and subtracting this rebuilt image from the original image removes the elliptically-symmetric bulge and disk components. This procedure leaves an image of the bar and spiral arms. Plotting the surface brightness of the fitted ellipses as a function of semi-major axis gives light-profiles, which were used to do a one-dimensional bulge-disk decomposition (see paper I).

### 3.2 Deprojection

The images were next deprojected, to remove the effects of galaxy inclination on the derived bar and arm parameters. Each galaxy was rotated so that its major axis was parallel with the y-axis of the Cartesian coordinate frame. The minor axis of the galaxy was then stretched along the x-axis by a factor determined by the ellipticity of the galaxy, resulting in the minor axis becoming equal to the major axis. The galaxies in the sample are either face-on or nearly face-on, so deprojection effects are small (typically the ratio of the minor-axis to the major-axis,  $b/a \simeq 0.8$ ).

### 3.3 Conversion to Polar Coordinates

Each of the deprojected difference images was converted from Cartesian to polar coordinates using a method similar to that of Elmegreen, Elmegreen & Montenegro (1992). The Cartesian image was mapped onto the new polar grid by calculating the Cartesian coordinates for each of the polar coordinate pixels. The number of counts associated with the calculated x-y position was then put in that polar coordinate position. The polar frame was divided into 540 steps of  $1^\circ$  in the  $\theta$  direction (i.e. wrapping around the galaxy one and a half times), and into 600 in the radial direction where 1 division was equal to  $0.01 \ln(r)$  and  $r$  is measured in pixels. This gave us sufficient oversampling to avoid loss of resolution even in the outer parts of the polar grid, and displaying one and a half turns makes it easier to identify spiral arms as continuous features.

### 3.4 Measurement of Spiral Pitch Angle

Spiral structure is assumed to have the form of a logarithmic spiral, given by

$$n\theta = \Lambda \ln \left( \frac{r}{r_0} \right) \quad (1)$$

where  $n$  is the number of arms,  $\theta$  is the azimuthal angle,  $\Lambda$  is a constant which defines the winding angle,  $r$  is radius and  $r_0$  is a scale length.

The pitch angle  $i$  is given by

$$\cot(i) = r \left| \frac{d\theta}{dr} \right|. \quad (2)$$

It can therefore be seen that

$$\cot(i) = \frac{\Lambda}{n} = \frac{d\theta}{d(\ln(r))} \quad (3)$$

i.e. the gradient of the arm in a  $\theta$  vs  $\ln(r)$  plot. This gradient was calculated by clicking along the ridge of the spiral arm with the cursor and fitting a straight line to these points. If the pitch angle of the arm changed with radius then we calculated an average pitch angle for that arm. Where galaxies had multiple arms the average pitch angle over all the arms was calculated. The errors in the pitch angle are calculated from the errors in the straight line fit, which is calculated using the residuals between the line and the data points. This is therefore dominated by the change in pitch angle with radius, in galaxies where this change is significant. The calculated pitch angles for all of the galaxies in this sample are listed in column 3 of table 1.

### 3.5 Measurement of Arm Strength

#### 3.5.1 Definition of Equivalent Angle

We have defined a new quantity, Equivalent Angle (EA), which parametrises the strength of arms, and was also used for bars in paper I. It is defined as the angle subtended by a sector of the disk which contains the same amount of flux as does the spiral arm, within the same radial limits. The advantage of using equivalent angle is that it is unaffected by seeing and other resolution effects unlike, for example, arm-interarm contrast (see paper I for a more detailed discussion).

#### 3.5.2 Calculation of Equivalent Angle

The polar coordinate images were used for the calculation of EA of spiral arms. Using the gradient of the arms (calculated whilst working out the pitch angle) the arms were transformed into horizontal features, by shearing columns of pixels according to the calculated gradient. Although this is not necessary here, it is necessary for calculating arm cross-sections (see section 3.6) and it also makes the calculation of arm EA easier. The arm was then divided into strips, each covering a small range in  $\ln(r)$ , and the equivalent angle was calculated for each strip, by dividing the arm flux by the flux from the rebuild image in the corresponding strip. In this way it was possible to calculate the equivalent angle as a function of radius for all of the galaxies in the sample.

The overall EA was calculated by taking the mean value of EA over the entire detectable range of the arm. The cutoff radii for this calculation are taken where the EA falls below  $3^\circ$ . The overall EA values are listed in column 4 of table 1.

#### 3.5.3 Arm Profiles

Figure 1 shows how arm EA varies with radius for four typical cases, NGC 1219, NGC 3512, UGC 11524 and IC 357. The start and end points are defined as in the previous section, except in the case of IC 357 where the starting point is at the end of the bar.

### 3.6 Calculation of Arm Cross-sections

Using the plots described in the previous section, where the arms are transformed into horizontal features, it is simple to calculate profiles across spiral arms by summing the flux in rows, i.e. along the arms. Figure 2 shows two such cross-sectional profiles (top row) for representative galaxies, with their decompositions into symmetric (middle row) and antisymmetric (bottom row) parts. Also shown in figure 2 is a  $540^\circ$  cut of IC 1809. The profiles can also be used to derive FWHM arm widths, measured in degrees of azimuthal angle, which are listed in column 6 of table 1. The errors on these FWHM depend on the errors on the measured gradients (i.e. pitch angles). With the error typically  $<5\%$  on the pitch angle it is found that the error on the FWHM is typically  $<10\%$ . This error has the effect of moving the peak of the cross-section by up to 10% and broadening the arm cross-section by 10% and this leads to an error in the calculated symmetries of  $\pm 5\%$ . Dividing these widths into the Equivalent Angle from column 4 of table 1 gives a good indication of the arm contrast, or degree of non-linearity, averaged along the arm. This is because EA is a measure of the flux in the arm with respect to the disk and the arm cross-section FWHM is a measure of the width of the arm in which this is contained. The shock strength is dependent upon the arm strength and we also expect stronger shocks in narrower arms. Therefore the ratio of arm EA to arm FWHM is a plausible indicator of the relative shock strengths in spiral arms.

The decomposition into symmetric and antisymmetric parts was performed using

$$I(r, \theta) = \frac{I(r, \theta) + I(r, 2\phi - \theta)}{2} + \frac{I(r, \theta) - I(r, 2\phi - \theta)}{2} \quad (4)$$

where the first and second terms represent the symmetric and antisymmetric parts, respectively, with respect to the position angle  $\phi$  of the major axis of the arm when plotted in  $\theta$  vs  $\ln(r)$  coordinates (Ohta, Hamabe & Wakamatsu 1990). The value of  $\phi$  was determined as being the data point that had the highest surface brightness. If there were two data points near the peak with similar surface brightness, then the value of  $\phi$  was taken to be half-way between these two points. When the value of  $\phi$  is changed by up to 2 pixels (the typical error in determining the value of  $\phi$ ) the asymmetries change by  $<2\%$ .

### 3.7 Fourier Analysis

#### 3.7.1 Method

We have measured the dominant modes of spiral structure in these galaxies using a simple Fourier technique adapted from the method used by González & Graham (1996). Three 10-pixel wide strips were taken along the  $\ln(r)$  coordinate of the  $\theta$  vs  $\ln(r)$  frame. These were binned up to create a

one-pixel-wide strip suitable for analysing with a 1-D Fast Fourier Transform (FFT) routine. The effect of smearing of the arms for a 10 pixel wide strip is small. An FFT of each of the strips was then taken, resulting in three power spectra, which were summed to increase the signal-to-noise ratio. As the FFT is taken over  $360^\circ$ , the power in all modes up to  $m = 360$  is calculated, although we are only interested in modes up to  $m \simeq 6$ . We average all the modes from  $m = 1$  to  $m = 6$  and quote the power of individual modes as a ratio with this average, in order to overcome any systematic noise effects (see section 3.7.2). The strongest mode for each galaxy in the sample is listed in column 6 of table 1. The relative strengths of all the modes are listed in table 2.

Figure 3a shows a histogram of the occurrence of the strongest mode in our sample with a subset in black indicating this for galaxies with near neighbours (see section 4.4 for a definition of near neighbours). Figure 3b shows the same histogram with a subset for the strongly barred galaxies, where a strongly barred galaxy is defined as a galaxy with a bar overall equivalent angle greater than the average for the whole sample (average bar EA=19.7°). These histograms will be discussed in section 4.

### 3.7.2 Discussion of Noise Effects

Fourier analysis can be subject to effects from noise, which may alter relative mode strengths (González & Graham 1996). We have investigated this problem in two ways, the first of which was to add a simulated noise frame to a  $\theta$  vs  $\ln(r)$  galaxy image, thereby doubling the pixel-to-pixel noise. Here, the image of IC 1764 was used. We found that the mode strengths were changed by  $< 5\%$  even under this significant noise increase.

For the second test, we simulated a strip of constant radius across a  $\theta$  vs  $\ln(r)$  image by adding together sine waves of different frequencies and introducing noise to this model. The input mode strengths were typical of those of our images. Even for models with pixel-to-pixel noise greater than our noisiest image, the FFT still finds the low order modes to have approximately the same power as was input. Thus it can be assumed that any noise has a small effect on the Fourier parameters presented here.

## 4 TESTING MODELS OF SPIRAL STRUCTURE

Having described the determination of all the necessary parameters from the near-IR images, we will now investigate the implications for various models of the formation of spiral structure in galaxy disks. This section is organised with each mechanism being discussed in turn, to see whether the new measurements support the mechanism as a strong contributor to the spiral structure. It should be noted that the various mechanisms discussed are by no means mutually exclusive, and it may be that several or all of them contribute at some level to the structures seen in spiral galaxy disks.

### 4.1 The Lin–Shu Hypothesis

#### 4.1.1 Spiral Pitch Angle

A fundamental prediction of the Lin–Shu hypothesis, and a central feature of the Hubble classification scheme, is that galaxies with greater mass concentration in their central bulges should have more tightly wound spiral structure. This can be demonstrated by the following back-of-envelope calculation. Lin & Shu (1964) derive the following expression for the locus of the spiral pattern,

$$n(\theta - \theta_0) = - \int_{r_0}^r \frac{[\kappa^2 + \omega_i^2 + (\omega_r - n\Omega)^2]}{(2\pi G\mu_0)} dr \quad (5)$$

where  $\theta$  is the azimuthal angle,  $\kappa$  is the epicyclic frequency,  $\mu_0$  is the fraction of mass in the disk,  $\Omega$  is the pattern speed and  $\omega_r$  and  $\omega_i$  are the real and imaginary parts, respectively, of the material speed.

Using equations 5 and 2,

$$\cot(i) = - \frac{1}{n} \frac{[\kappa^2 + \omega_i^2 + (\omega_r - n\Omega)^2]}{2\pi G\mu_0} \quad (6)$$

Equation 6 contains the desired result, that galaxies with more dominant disks should have spiral structure that is more loosely wound. Roberts et al. (1975) converted this into a correlation between pitch angle and Hubble type, which they assumed to be essentially determined by bulge-to-disk ratio. They calculated the theoretical winding angle from the bulge-to-disk ratios of a sample of galaxies and plotted this versus Hubble type. The line drawn in figure 5 is their predicted correlation. Roberts et al. (1975) also state that although the pitch angle has some dependence on the dynamical properties of the disk, e.g.  $\kappa$ ,  $\omega_i$  and  $\omega_r$  in equation 6 above, its dependence upon the fraction of mass in the disk is stronger. The dynamical properties, especially the material speed, seem to correlate more strongly with the luminosity class (van den Bergh 1960) of the galaxy than with Hubble type.

Kennicutt (1981) found only weak correlations between pitch angle and Hubble type, and between pitch angle and bulge-to-disk ratio. He also found a correlation between pitch angle and the maximum rotational velocities of spiral galaxies. This seems inconsistent with spiral density wave theories as it shows that arm strength reflects the effects of differential rotation. Kennicutt (1982) found that arm width increases smoothly with galaxy luminosity, with a slope consistent with broadening by galactic rotation (i.e. galaxies with larger rotation speeds have broader arms). This is consistent with the luminosity class (van den Bergh 1960) being dependent upon dynamical properties of galaxies (Roberts et al. 1975). Kennicutt & Hodge (1982) measured pitch angles of 17 galaxies from the sample of Roberts et al. (1975) using H $\alpha$  data. They found that their measured pitch angles correlated well with the Roberts et al. (1975) model pitch angles, but that the model systematically underestimated all the pitch angles. These authors' work was performed using B-band and H $\alpha$  data which is strongly affected by young stars, and so we have performed this using K-band data, which is known to have a significantly different morphology from optical wavebands (e.g. Block et al. 1994).

We can directly test the important prediction of a correlation between mass concentration and winding angle using our images. The pitch angle (equation 2) quantifies how tightly wound spiral structure is, where small pitch angles

imply tightly wound structure. To parametrise the central mass concentration we used the fraction of K-band light in the disk ( $L_{\text{disk}}/(L_{\text{disk}} + L_{\text{bulge}})$ ), calculated by numerical integration over the profiles, from the galaxy centre to beyond the edge of the observed galaxy, for both bulge and disk. This parameter is listed in column 7 of table 1. (We use this parameter rather than the more widely used bulge-to-disk ratio for consistency with Lin & Shu 1964.)

A plot of pitch angle versus the fraction of light in the disk (shown in figure 4) shows no correlation of the type predicted by Lin & Shu (1964). Figure 5 shows a plot of pitch angle against Hubble type, which also lacks any correlation and is in very clear disagreement with the line derived from the predictions of Roberts et al. (1975).

There is an even simpler test which demonstrates that spiral arms cannot have the fixed form indicated by equation 6. The lack of any  $\theta$ -dependence predicts that the arms in any spiral galaxy should have the same pitch angle at any given radius, in the Lin-Shu model. This can be tested by looking at  $\theta$  vs  $\ln(r)$  images of galaxies, where the pitch angle can be determined directly from the gradient of the arms. This test is completely independent of the radial variation of dynamical properties. Figure 6 shows a contour plot of the galaxy NGC 2503, demonstrating that the two arms have very different gradients, and therefore pitch angles, at the same radius. This occurs in 20 out of the 45 galaxies in our sample, and is also seen clearly in the  $\theta$  vs  $\ln(r)$  image of M99 presented by González & Graham (1996). Of these 20 galaxies, 9 have strong  $m=1$  modes, i.e. a degree of lopsidedness, which can produce variations in pitch angle. This is seen in galaxies which have a bulge which is offset from the centre of the disk as seen in UGC 3900 (see figure 8). Both this and the fact that pitch angle does not correlate with Hubble type or B/D ratio seem to suggest that the simplest form of density wave theory is at least incomplete. Indeed, it is not clear that a superposition of spiral waves, as postulated by modal theories, can produce this type of azimuthal variation in arm properties, which is most easily reconciled with SSPSF models.

We find the lack of any correlation between spiral winding angle and Hubble type quite surprising. In paper I we found that Hubble type correlates only weakly with bulge-to-disk ratio (B/D), and we now find no correlation with arm morphology, at least in the near-IR, raising the question of what does determine Hubble type. Other recent studies have found that the bulge surface brightness correlates strongly with Hubble type (de Jong 1996b) suggesting that only bulge parameters are important in determining Hubble type.

Another possibility is that the mass of cold gas plays a key role in determining galaxy type. This is consistent with arguments of Block & Wainscoat (1991) and Block et al. (1994) who find that the Population I disk of young stars, which dominates the optical appearance, can be largely decoupled from the distribution of older stars. This can explain the discrepancy between our findings and the optical study of Kennicutt (1981). (Note, however, that in section 5.1 we will report reasonably good agreement between arm morphologies for 3 of our galaxies imaged in both the B and K bands, so this decoupling cannot be complete.)

#### 4.1.2 Arm Cross-Sections

We now consider cross-sections through spiral arms illustrated for some of the more strongly-armed galaxies in figure 2, and the implications of these for density wave theories.

Figure 2 shows that arm cross-sections for strong arms are typically asymmetric at only the 5-10% level, which is consistent with density wave theory, assuming that the K-band light traces the stellar mass density and is largely unaffected by extinction and the shocks which perturb the gas density. However, the Lin-Shu hypothesis predicts that density waves are sinusoidal in nature with a  $180^\circ$  period, leading to a FWHM of  $60^\circ$  for each arm of a 2-armed spiral (c.f.  $120^\circ$  for a one-armed mode,  $40^\circ$  for 3-armed,  $30^\circ$  for 4-armed etc). The measured FWHM of the arm cross-sections vary between  $10^\circ$  and  $70^\circ$  with typical values in the range  $20^\circ$ - $40^\circ$  (see column 6 of table 1). Thus the arms are almost always narrower than expected for grand-design 2-armed structure, and in most cases  $\sim 25\%$  narrower than expected on the basis of the dominant Fourier mode of the galaxy. The typical error on the FWHM is  $<10\%$  and the typical error on the asymmetries is 5%. The  $540^\circ$  cut of IC 1809 also demonstrates that arm cross-sections are not sinusoidal. There are two possible explanations for this, the first of which is that the Lin-Shu hypothesis may be oversimplistic (see section 4.2). The other explanation may be that the arms are narrower due to the effect of young supergiant stars forming near the peak of the density wave. Rix & Rieke (1993) showed that the affect of supergiants is small for M51, but Rhoads (1998) has shown that supergiant stars contribute up to 30% of the local luminosities, which may have the effect of making arms appear somewhat narrower than predicted by the Lin-Shu hypothesis.

Figure 15 shows K-band arm cross-sections for the galaxies for which we have B-band data. These cross-sections appear less symmetrical than those shown in figure 2. However, the galaxies in figure 2 have strong spiral structure, whereas those in figure 15 have arms that are weaker and the profiles are thus somewhat noisier. The asymmetries for these less strongly-armed spirals are at about the 25% level.

## 4.2 Modal Theories

### 4.2.1 Fourier Analysis

The narrowness of the arm cross-sections (shown in figure 2 and described above) can be explained by modal theory (Bertin & Lin 1996; Bertin et al. 1989a, 1989b), where higher order modes can be superposed on the  $m = 2$  mode resulting in narrower arms. The presence of such multiple modes can be tested using Fourier decomposition of the disk structure. Although low-order modes are expected to be dominant, high-order modes should also be present but with weaker amplitudes.

It can be seen from figure 3a that the most common dominant modes in the sample are  $m = 1$  and  $m = 2$ , each of which dominates the disk structure of about one-third of the galaxies, whilst the  $m = 4$  mode accounts for most of the remainder (a quarter of the total). The  $m = 3$  mode dominates in only 4 out of 45 cases, and the relative weakness of the  $m = 3$  mode is probably the strongest result of this analysis.

Rix & Zaritsky (1995) performed a Fourier analysis of

18 face-on spirals, imaged in the K band. They found that about half of the galaxies in their sample had a strong two-armed spiral component with an arm-interarm contrast of about 2:1 and consequently strong  $m = 2$  and  $m = 4$  modes. González & Graham (1996) performed a detailed study of the galaxies M99 and M51 including a Fourier analysis of both galaxies. They looked at the dependence of  $m = 1$  to  $m = 6$  modes with radius and found that the  $m = 2$  mode was the strongest at all radii in the grand-design spiral M51, and that M99 was dominated by the  $m = 2$  mode at most radii. This was found to be true in both optical and K-band images of M99. Analysis of a sample of seven galaxies in the K'-band ( $2.1\mu\text{m}$ ) reported by Block et al. (1994) finds structure dominated by the  $m = 1$  and  $m = 2$  modes, with the lack of higher modes being attributed to damping of such modes in the old stellar disk by the Inner Lindblad Resonance (ILR).

We can therefore conclude that the frequent occurrence of the low order  $m = 1$  and  $m = 2$  modes is in agreement with predictions from modal theories, as is the suppression of the  $m = 3$  mode. The dominance of the  $m = 4$  mode in 9 out of 45 cases, however, cannot be explained by modal theories, which predict that such modes should be damped by the ILR.

#### 4.2.2 Arm Profiles

The arm profiles of the galaxies NGC 1219 and NGC 3512 (shown in figure 1) show some evidence for modulation (Bertin & Lin 1996; Bertin et al. 1989a, 1989b), i.e. peaks and troughs in the radial light profiles of arms of spiral galaxies. These authors interpret modulation as the result of interference between different wave packets within the disk of the galaxy. Our measurement of the same effect in K-band images demonstrates that this is not simply due to extinction, but represents a true modulation in arm strength. Of the 16 galaxies with sufficiently long and strong arms to test clearly for this effect, 4 show clear modulation and a further 6 show some indication of such effects.

These modulation effects are superimposed on arm profiles generally showing an increase in EA at small radii, which then turns over and decreases. This implies that in the inner disk, the scale length of the arms is greater than that of the disk (i.e. the arm surface brightness falls off less rapidly than the disk surface brightness) and in the outer disk the scale lengths of arms are smaller than disk scale lengths. This is in agreement with the result of González & Graham (1996) who found a peak in the arm-interarm contrast at intermediate radii.

### 4.3 Driving by Bars

#### 4.3.1 Testing models of bar-driven spiral structure

Bars may be responsible for the driving of spiral structure (Sanders & Huntley 1976) but Sellwood & Sparke (1988) have shown that that bar driving is only important for the most strongly-barred spiral galaxies. In addition, it is thought that bar forcing should not extend far outside the region where the bar potential is strong (Sanders & Tubbs 1980).

We have tested models of bar-driven spiral structure

by looking for a correlation between bar strength and arm strength. The result of this can be seen in figure 7, which shows a plot of arm strength in the inner part of the disk against bar strength. There is no correlation. It would therefore appear that bars do not strongly affect the strength of spiral arms, even in the central regions of disks.

#### 4.3.2 Results of the Fourier Analysis

Figure 3b shows enhancement of the  $m = 3$  and  $m = 4$  modes for galaxies that we have classed as strongly barred, relative to the sample as a whole. A Kolmogorov-Smirnov (KS) test showed that this result is not significant. If this result is confirmed by analysing larger samples of galaxies in the same way, then it would be surprising as bar-driven models predict strong 2-armed spiral structure (e.g. Sanders & Huntley 1976; Sanders 1977).

#### 4.3.3 Relation Between Arm Morphology and Bars

The relation between the morphology of bars and arms has been discussed by Sellwood & Sparke (1988), who claim that bars and arm structures may have different pattern speeds. If this were the case then galaxies would sometimes have arms starting ahead of the bar ends, although their simulations show that this should not happen very often. They find that in 100 time steps of their model there are two steps for which the ends of bars and the beginnings of arms do not meet. We have observed this behaviour in 2 out of 15 strongly barred galaxies. Our image of UGC 3900 (figure 8) shows quite evidently that its arms do not start at the end of the bar, and IC 568 shows a similar morphology. The qualitative agreement between the appearance of these galaxies and the simulations is very good, but it may happen somewhat more frequently than predicted by Sellwood & Sparke (1988).

### 4.4 Testing models of spiral structure involving tidal interactions

Kormendy & Norman (1979) proposed an alternative explanation to spiral density waves for the maintenance of global spiral structure. Noting that the 'spiral winding problem' is only actually a problem in the differentially rotating parts of disks, they postulated that grand-design structure may only occur in one of two situations. Firstly, some galaxies may have grand-design spiral structure only within the radius within which solid body rotation occurs, and thus completely avoid the 'spiral winding problem'. Kormendy and Norman then claim that galaxies exhibiting grand-design spiral structure outside this radius could be undergoing tidal interactions with other nearby galaxies, or be strongly barred. In these cases the driving field from the neighbour or bar maintains spiral structure even in the regions of the disk subject to differential rotation (although note our conclusion in section 4.3.1). Studying a sample of 54 galaxies, they found that 45 exhibited global spiral patterns, and of these, only two clearly show global spiral structures in the differentially-rotating part of the disk, with no bars or neighbours to provide a driving field. All others fitted into the proposed model.

Observational support for this view has been provided

by Elmegreen, Seiden & Elmegreen (1989) who observed that, generally, grand-design spiral galaxies are found in richer environments than flocculent spirals (i.e. grand-design spiral structure galaxies are more likely to have undergone a tidal interaction with another galaxy in their history). We now test these results with our data.

Kormendy & Norman (1979) define a tidally-significant neighbour galaxy as one within 3–5 galaxy diameters and 1 magnitude (V-band) of the spiral galaxy in question. We have relaxed this somewhat to 6 diameters because few of the galaxies in our sample meet the more stringent criterion, which is, in any case, somewhat arbitrary, particularly since there is time for galaxies to move apart between the time of interaction and the development of spiral structure. We performed a search for near neighbours using the Digitised Sky Survey and diameters ( $B_{25}$ ) from the RC3. The apparent visual magnitudes of the near neighbours are comparable to those of the sample galaxies.

Figure 9 shows a histogram of the distribution of arm strengths (in terms of equivalent angle) in the whole sample with the galaxies with near neighbours indicated in black. It can be seen that 4 out of 7 galaxies with arm equivalent angle greater than  $35^\circ$  have near neighbours whereas only 12 out of 45 galaxies in the sample have companions. Whilst a KS test shows that this difference is not statistically significant due to the small numbers involved, there is some indication here of a relation between arm strength and tidal interactions. This conclusion is strengthened by figure 3a which shows that the presence of near neighbours enhances the  $m = 2$  mode, with this being the dominant mode in 7 out of 12 galaxies with nearby neighbours, compared to only 7 out of 33 galaxies with no apparent neighbours.

Figure 10 shows a histogram of the distribution of the total azimuthal angle over which the strongest arm of each galaxy in our sample can be detected, both for the whole sample and the galaxies with near neighbours (black). This figure shows no evidence of near neighbours enhancing global modes which would be represented by longer spiral arms subtending larger azimuthal angles.

It therefore seems that the presence of nearby galaxies may affect the strength of arms and enhance the  $m = 2$  mode, but they have no effect on the angular extent over which arms can be detected. This provides some support for the model presented by Kormendy and Norman (1979), but they also require driving by bars to be efficient at generating and maintaining global arm structures, and we find no evidence for this effect (section 4.3.1).

#### 4.5 Arm Strengths as a Function of the Underlying Galaxy Properties

Kormendy & Norman (1979) claim that a dominant bulge will prevent the formation of global spiral arms in galaxies due to the differential rotation caused by a strong central mass concentration. We can test this by determining the azimuthal angle that arms subtend as a function of bulge-to-disk ratio. This is plotted in figure 11, which shows a hint of a deficit of global arm structures for galaxies with dominant bulges, i.e. no points lying in the upper right-hand corner of the plot. This is consistent with the predictions of Kormendy & Norman (1979).

Toomre (1964) claimed that galaxies with heavier disks

are more unstable to perturbations. Galaxies with heavier disks should have brighter disk central surface brightnesses and if these ‘heavy disks’ were more unstable we would expect to obtain larger arm equivalent angles for them. Figure 12 shows a plot of arm equivalent angle against disk central surface brightness. No correlation is shown but there does seem to be a lack of low-surface-brightness galaxies with large arm EA.

## 5 RELATION BETWEEN ARM STRENGTH AND STAR FORMATION

In this section we try to distinguish between the two main theories for the occurrence of star-formation in spiral galaxy disks. The first of these is the Large Scale Shock Scenario (Roberts 1969), which predicts that as gas moves through the density wave it becomes shocked and star formation results. In this case star formation rate depends on the strength of the shock and thus should correlate with measured arm strength. However, Elmegreen & Elmegreen (1986) claim that density waves cannot trigger star formation because their contrast above the disk is not high enough. They suggest that although density waves are responsible for organising material in spiral arms, some other mechanism must be responsible for forming stars. Sleath & Alexander (1995, 1996) suggest that this mechanism is Stochastic Self Propagating Star Formation (Gerola & Seiden 1978). In this type of model, no strong correlation would be expected between arm strength and star formation rate in the disk.

We have used the IRAS  $60\mu\text{m}$  and  $100\mu\text{m}$  fluxes to calculate the far-infrared luminosity for the galaxies in our sample for which IRAS data was available. The far-infrared luminosity can be used as a quantitative indicator of star-formation rates (e.g. Spinoglio et al. 1995). This was divided by the K-band luminosity of the galaxies to compensate for differences in their overall size, and then compared with their overall arm strengths in EA normalised to the arm FWHM to see if shocks in the arms are triggering the formation of stars. The far-infrared luminosity in terms of the  $60\mu\text{m}$  and  $100\mu\text{m}$  flux is given by Lonsdale et al. (1985) as

$$L_{FIR} = 3.75 \times 10^5 D^2 (2.58S_{60} + S_{100}) \quad (7)$$

where  $L_{FIR}$  is the far-infrared luminosity in solar units,  $D$  is the distance to the galaxy in Mpc,  $S_{60}$  is the  $60\mu\text{m}$  flux in Jy and  $S_{100}$  is the  $100\mu\text{m}$  flux in Jy.

Figure 13 shows a plot of the far-infrared luminosity normalised to K-band luminosity against the overall EA to arm FWHM ratio. The correlation coefficient is 0.79 at a significance level of 99.8%. The error bars here are calculated from the errors on the IRAS fluxes found using NED. IC 568 (denoted by a hollow circle) was found to have a starburst nucleus on the basis of a very red nuclear colour (Paper I), and this undoubtedly contributes to the high FIR luminosity. It was omitted from the calculation of the correlation coefficient given above.

If the large-scale shock scenario (Roberts 1969) is correct a strong correlation between arm strength (or the strength of shocks in the arms) and star-formation rate would be expected. Knapen & Beckman (1996) find both star-formation rates and star formation efficiencies are enhanced in the arms compared to the interarm regions of

M101 and this supports the Large Scale Shock Scenario. Figure 13 shows that we also find a good correlation, in the expected sense.

### 5.1 Comparison of B-band data with K-band data

Additional B-band images were obtained for the galaxies NGC 5478, UGC 6958 and UGC 8939. The dominant source of blue light is young bright stars and so these data can be used to investigate the dependence of star formation on the underlying spiral density perturbation. The B-band images were taken at the SAAO 1m Elizabeth telescope with a 512x512 TEK8 CCD, and were reduced and analysed in an essentially identical manner to that for the K-band data. Here we compare the arm profiles, cross-sections and pitch angles derived from K-band images with the same parameters from B-band data

Table 3 shows a comparison for the overall arm strengths between the K-band data and B-band data. For the strongly armed galaxies (NGC 5478 and UGC 6958) the K-band arms are stronger than the B-band arms. However, for UGC 8939 (which has weak arms) the B-band arms are stronger than the K-band arms. In our search for near neighbours we found that UGC 8939 has two near neighbours at a distance of about 2 galaxy diameters and with similar surface brightnesses to UGC 8939. It may be that the companion galaxies are affecting the star-formation rate in UGC 8939, thus causing its B-band arms to appear stronger than its K-band arms.

If the large scale shock scenario (Roberts 1969) and the Lin-Shu hypothesis (Lin & Shu 1964, 1966) are correct we expect gas to approach the arm from the concave side, assuming arms are trailing and that the area under consideration is within corotation. The gas will then be compressed and, if the perturbation is strong enough, shocked at the centre of the arm, leading to subsequent star formation. Thus we should see star formation on the leading, convex edges of spiral arms, within the corotation radius. Observationally, this should result in B-band arms leading K-band arms. In order to test this we have compared the azimuthal angles at the start of the arms, and the pitch angles, for the B-band and K-band images. (Note that the image of UGC 6958 was first flipped to make the arms spiral outwards in a clockwise direction, consistent with the other two galaxies.) Table 4 shows the results of this analysis. Figure 14 also shows a plot of the difference between the azimuthal angle of the K-band arm and that of the B-band arm for UGC 8939 as radius increases. It can be seen that, generally, the B-band arms lead K-band arms by an average azimuthal angle of  $\simeq 5^\circ$  at low radii increasing to 10s of degrees at high radii. This result and table 4 show that K-band arms are more tightly wound than B-band arms for UGC 8939. Similar plots for UGC 6958 and NGC 5478 (not shown), whilst noisier, show some tendency for K-band arms to have smaller pitch angles than B-band arms. This confirms the result of Kennicutt (1981) who used B-band and R-band optical data. This therefore seems to confirm the Large Scale Shock Scenario. However, there is another possible explanation. Visible images show dust lying preferentially on the trailing edges of arms, which would also result in B-band arms appearing to lead K-band arms as a result of the increased extinction at B. However, the fact that dust lanes appear on the trailing

edges of arms is in itself evidence for the Large Scale Shock Scenario (Roberts 1969) since dust lanes are conventionally taken as tracers of shocks.

Figure 15 shows a comparison of B- and K-band arm cross-sections. In general it can be seen that the FWHM of the cross-sections of B-band arms are much smaller than those of K-band arms. There could be a number of factors contributing towards this. In the B-band (or any visible waveband) spiral arms are defined by the narrow regions where stars are formed and this may be contributing to the low FWHM of B-band arms. In addition, B-band arms are frequently observed to bifurcate into smaller, narrower arms. Finally, blue light is strongly affected by dust which lies predominantly on one side of spiral arms and would therefore have the effect of making B-band arms appear narrower than K-band arms.

## 6 CONCLUSIONS

We now summarise the implications of these observations for the main models of the formation and stability of spiral structure. No one theory fits all of the observations, but a combination can explain most or all of the features we have observed. This section summarises these conclusions.

Simple density wave theories (e.g. Lin & Shu 1964, 1966) are undermined in three ways. Firstly, we do not get the correlation between the fraction of light in the disk and pitch angle which is predicted by Lin & Shu (1964) and Roberts et al. (1975). Secondly, Lin & Shu (1964) predict that pitch angle should be the same for arms at the same radius within a given galaxy. We find that this is not the case. Finally, we have found that the FWHM of arm cross-sections are somewhat narrower than predicted by simple density wave theories.

More complicated density wave theories, e.g. Modal theory (Bertin et al. 1989a, 1989b; Bertin & Lin 1996), are supported by modulation effects that we have found in arm strength as a function of radius, and which appear to be fairly common.

Bar driven models of spiral structure (Sellwood & Sparke 1988; Sanders & Huntley 1976) are not supported by our observations, as we find no correlation between arm strength and bar strength, even in the inner part of the disk.

Tidal effects from near neighbours seem to have some effect. We find that 4 out of 7 galaxies with arm EA greater than  $35^\circ$  have near neighbours whereas only 12 out of 45 galaxies in whole sample have near neighbours. We also find that in the Fourier analysis of galaxies with near neighbours, the even low-order modes are dominant, especially the  $m = 2$  mode.

We have also discussed factors affecting star formation in the disks of spiral galaxies. We have found evidence both for and against the Large Scale Shock Scenario (Roberts 1969). Firstly, we find a correlation between arm contrast and the normalised star formation rate, in agreement with the predictions of the large scale shock scenario. Secondly, we find that B-band arms are more loosely wound and narrower than K-band arms, confirming the predictions made by density wave theories (Roberts 1969). However, this can also be interpreted as an extinction effect because dust lies on the trailing edges of arms.



Finally, and possibly most significantly, we find no correlation between the arm properties of this sample of galaxies and their classified Hubble type. Combining this with the poor correlation between Hubble type and K-band B/D ratio (Paper I), it would appear impossible to allocate a Hubble type to these galaxies on the basis of these K-band observations, and the morphology of the old stellar population varies surprisingly little between Hubble types Sa and Sd. We speculate that the determining parameter for Hubble type is cold gas content, which controls the star formation rate and the distribution of the young stars, which dominate the optical appearance.

## 7 ACKNOWLEDGEMENTS

We thank Paul Lynam for the B-band images, taken at the 1m Elizabeth telescope at SAAO. We also wish to acknowledge Debra Elmegreen and Frederick Chromey for useful suggestions, and John Porter for his comments on an early draft of this paper. The United Kingdom Infrared Telescope is operated by the Joint Astronomy Centre on behalf of the U.K. Particle Physics and Astronomy Research Council. This research has made use of the NASA/IPAC Extragalactic Database (NED), which is operated by the Jet Propulsion Laboratory, California Institute of Technology, under contract with the National Aeronautics and Space Administration. We thank the referee for many helpful suggestions which improved the content and presentation of this paper.

## REFERENCES

Bertin G., Lin C.C., 1996, *Spiral Structure in Galaxies - A Density Wave Theory*, MIT Press, Cambridge Massachusetts  
 Bertin G., Lin C.C., Lowe S.A., Thurstans R.P., 1989a, *ApJ*, 388, 78  
 Bertin G., Lin C.C., Lowe S.A., Thurstans R.P., 1989b, *ApJ*, 388, 104  
 Block D.L., Wainscoat R.J., 1991, *Nat*, 353, 489  
 Block D.L., Bertin G., Stockton A., Grosbøl P., Moorwood A.F.M., Peletier R.F., 1994, *A&A*, 288, 365  
 de Jong R.S., 1996b, *A&A*, 313, 377  
 de Vaucouleurs G., de Vaucouleurs A., Corwin H.G. Jr, Buta R.J., Paturel G., Fouqué P., 1991, *The Third Reference Catalogue of Bright Galaxies*, Univ. Texas Press, Austin (RC3)  
 Elmegreen B.G., Elmegreen D.M., 1986, *ApJ*, 311, 554  
 Elmegreen B.G., Elmegreen D.M., Chromey F.R., Hasselbacher D.A., Bissell B.A., 1996, *AJ*, 111, 2233  
 Elmegreen B.G., Elmegreen D.M., Montenegro L., 1992, *ApJS*, 79, 37  
 Elmegreen B.G., Seiden P.E., Elmegreen D.M., 1989, *ApJ*, 283, 251  
 Gerola H., Seiden P.E., 1978, *ApJ*, 223, 129  
 González R.A., Graham J.R., 1996, *ApJ*, 460, 651  
 Kennicutt R.C., 1981, *AJ*, 86, 1847  
 Kennicutt R.C., 1982, *AJ*, 87, 255  
 Kennicutt R.C., Hodge P., 1982, *ApJ*, 253, 101  
 Knapen J.H., 1993, *PASP*, 105, 323  
 Knapen J.H., Beckman J.A., 1996, *MNRAS*, 283, 251  
 Kormendy J., Norman C.A., 1979, *ApJ*, 233, 539  
 Lin C.C., Shu F.H., 1964, *ApJ*, 140, 646  
 Lin C.C., Shu F.H., 1966, *Proc. Nat. Acad. Sci.*, 55, 229  
 Lin C.C., Yuan C., Shu F.H., 1969, *ApJ*, 155, 721

Lonsdale C.J., Helou G., Good J.C., Rice W.L., 1985, *Catalogued Galaxies and Quasars Observed in the IRAS Survey*, Washington D.C.  
 Nakai N., Kuno N., Handa T., Sofue Y., 1994, *PASJ*, 46, 527  
 Ohta K., Hamabe M., Wakamatsu K.-I., 1990, *ApJ*, 357, 71  
 Rand R.J., 1993, *ApJ*, 410, 68  
 Rand R.J., 1995, *AJ*, 109, 2444  
 Regan M.W., Vogel S.N., 1995, *ApJ*, 452, 21  
 Reuter H.-P., 1996, *A&A*, 306, 721  
 Rhoads J.E., 1998, *AJ*, 115, 472  
 Rix H.-W., Rieke M.J., 1993, *ApJ*, 418, 123  
 Rix H.-W., Zaritsky D., 1995, *ApJ*, 447, 82  
 Roberts W.W., 1969, *ApJ*, 74, 859  
 Roberts W.W., Roberts M.S., Shu F.H., 1975, *ApJ*, 196, 381  
 Sanders R.H., 1977, *ApJ*, 216, 916  
 Sanders R.H., Huntley J.M., 1976, *ApJ*, 209, 53  
 Sanders R.H., Tubbs A.D., 1980, *ApJ*, 235, 803  
 Seigar M.S., James P.A., 1998, *MNRAS*, submitted (paper I)  
 Sellwood J.A., Sparke L.S., 1988, *MNRAS*, 231, 25p  
 Sleath J.P., Alexander P., 1995, *MNRAS*, 275, 507  
 Sleath J.P., Alexander P., 1996, *MNRAS*, 283, 358  
 Spinoglio L., Malkan M.A., Rush B., Carrasco L., Recillas-Cruz E., 1995, *ApJ*, 453, 616  
 Tilanus R.P.J., Allen R.J., 1991, *A&A*, 244, 8  
 Tilanus R.P.J., Allen R.J., 1993, *A&A*, 274, 707  
 Toomre A., 1964, *ApJ*, 139, 1217  
 Toomre A., Toomre J., 1972, *ApJ*, 178, 623  
 van den Bergh S., 1960, *ApJ*, 131, 215  
 Visser H.C.D., 1980, *A&A*, 88, 159

**Table 1.** Summary of the arm and disk properties of the 45 galaxies. The Hubble types of the galaxies are listed in column 2; the measured pitch angles of the spiral arms, averaged over the number of arms, with the radial extent over which this is measured in arcsec are listed in column 3; the overall arm strengths, with the number of arms used to calculate this average in brackets, in column 4; the dominant mode of the spiral structure in column 5; the arm cross section full width at half maximum (FWHM) in column 6; the fraction of light in the disk in column 7 and the azimuthal angle subtended by the strongest arm in column 8.

Galaxy Name	Hubble type	Pitch angle	Overall EA (no. arms)	Dominant Fourier mode, m	Arm FWHM	Fraction of light in disk	Azimuthal angle subtended by arm in degrees
ESO 555 -G 013	Sa	$6.3^{\circ} \pm 0.7$ (7, 11)	$19^{\circ} \pm 5$ (2)	2	$18^{\circ}$	–	49
IC 357	SBab	$8.3^{\circ} \pm 0.8$ (17, 23)	$49^{\circ} \pm 7$ (2)	4	$15^{\circ}$	0.74	45
IC 568	SBb	$8.4^{\circ} \pm 0.7$ (16, 24)	$26^{\circ} \pm 4$ (2)	2	$18^{\circ}$	0.68	32
IC 742	SBab	$9.3^{\circ} \pm 1.4$ (13, 17)	$13^{\circ} \pm 3$ (2)	1	$20^{\circ}$	0.83	30
IC 1196	Scd	$15.8^{\circ} \pm 1.3$ (13, 21)	$11^{\circ} \pm 2$ (2)	1	$18^{\circ}$	0.67	57
IC 1764	SBb	$10.2^{\circ} \pm 0.6$ (15, 25)	$18^{\circ} \pm 4$ (1)	2	$48^{\circ}$	0.78	31
IC 1809	SBab	$9.9^{\circ} \pm 0.7$ (7, 20)	$28^{\circ} \pm 2$ (2)	4	$18^{\circ}$	0.52	115
IC 2363	SBbc	$9.8^{\circ} \pm 0.7$ (12, 20)	$25^{\circ} \pm 5$ (3)	4	$28^{\circ}$	0.76	36
IC 3692	SBa	$6.5^{\circ} \pm 1.0$ (15, 20)	$11^{\circ} \pm 3$ (2)	1	$8^{\circ}$	0.70	88
NGC 1219	SAbc	$6.5^{\circ} \pm 2.0$ (8, 21)	$9^{\circ} \pm 2$ (2)	4	$17^{\circ}$	0.84	89
NGC 2416	Scd	$9.1^{\circ} \pm 0.8$ (12, 22)	$37^{\circ} \pm 6$ (2)	1	$17^{\circ}$	0.94	85
NGC 2503	SABbc	$6.1^{\circ} \pm 1.1$ (11, 19)	$19^{\circ} \pm 2$ (2)	4	$26^{\circ}$	0.89	64
NGC 2529	SBd	$10.0^{\circ} \pm 0.5$ (10, 22)	$31^{\circ} \pm 2$ (2)	1	$50^{\circ}$	0.9	83
NGC 2628	SABc	$9.4^{\circ} \pm 1.1$ (8, 27)	$12^{\circ} \pm 4$ (3)	2	$30^{\circ}$	0.9	107
NGC 3512	SABc	$10.2^{\circ} \pm 0.9$ (11, 29)	$12^{\circ} \pm 2$ (2)	1	$49^{\circ}$	0.92	173
NGC 5478	SABbc	$9.2^{\circ} \pm 1.2$ (6, 18)	$37^{\circ} \pm 2$ (2)	1	$36^{\circ}$	0.73	93
NGC 5737	SBb	$9.4^{\circ} \pm 0.7$ (13, 22)	$13^{\circ} \pm 1$ (2)	4	$32^{\circ}$	0.76	95
NGC 6347	SBb	$8.0^{\circ} \pm 0.8$ (5, 12)	$11^{\circ} \pm 2$ (3)	4	$38^{\circ}$	0.93	200
NGC 6379	Scd	$8.7^{\circ} \pm 0.5$ (10, 23)	$18^{\circ} \pm 7$ (2)	1	$24^{\circ}$	0.86	83
NGC 6574	SABbc	$9.9^{\circ} \pm 1.4$ (11, 28)	$6^{\circ} \pm 3$ (3)	1	$20^{\circ}$	0.87	55
UGC 850	SAbc	$4.8^{\circ} \pm 0.3$ (4, 16)	$18^{\circ} \pm 1$ (2)	2	$30^{\circ}$	0.84	310
UGC 1478	SBc	$12.2^{\circ} \pm 0.5$ (8, 24)	$39^{\circ} \pm 4$ (2)	1	$21^{\circ}$	0.74	54
UGC 1546	SABc	$8.0^{\circ} \pm 0.4$ (3, 15)	$12^{\circ} \pm 2$ (1)	2	$17^{\circ}$	0.84	176
UGC 2303	SABb	$4.1^{\circ} \pm 0.5$ (8, 13)	$9^{\circ} \pm 1$ (3)	3	$50^{\circ}$	0.74	125
UGC 2585	SBb	$4.6^{\circ} \pm 0.5$ (14, 17)	$26^{\circ} \pm 1$ (1)	2	$22^{\circ}$	0.74	54
UGC 2705	SBcd	$7.7^{\circ} \pm 1.0$ (4, 24)	$14^{\circ} \pm 2$ (3)	3	$44^{\circ}$	0.66	184
UGC 2862	SABa	$6.9^{\circ} \pm 0.4$ (5, 13)	$10^{\circ} \pm 2$ (1)	3	$38^{\circ}$	0.34	76
UGC 3053	Scd	$8.6^{\circ} \pm 0.3$ (7, 16)	$8^{\circ} \pm 2$ (3)	1	$28^{\circ}$	0.94	114
UGC 3091	SABd	$9.1^{\circ} \pm 0.9$ (5, 10)	$8^{\circ} \pm 2$ (2)	1	$43^{\circ}$	0.87	101
UGC 3171	SBcd	$12.9^{\circ} \pm 0.4$ (5, 11)	$10^{\circ} \pm 3$ (2)	1	$32^{\circ}$	0.96	190
UGC 3233	Scd	$9.0^{\circ} \pm 1.6$ (7, 10)	$5^{\circ} \pm 1$ (2)	2	$47^{\circ}$	0.75	69
UGC 3296	Sab	$10.5^{\circ} \pm 1.4$ (14, 20)	$6^{\circ} \pm 1$ (3)	2	$33^{\circ}$	0.88	63
UGC 3578	SBab	$9.3^{\circ} \pm 0.6$ (15, 32)	$24^{\circ} \pm 9$ (2)	2	$19^{\circ}$	0.74	71
UGC 3707	Sab	$7.0^{\circ} \pm 1.4$ (15, 19)	$33^{\circ} \pm 4$ (2)	1	$22^{\circ}$	0.73	17
UGC 3806	SBcd	$5.8^{\circ} \pm 0.3$ (8, 30)	$8^{\circ} \pm 2$ (2)	1	$26^{\circ}$	0.93	72
UGC 3839	SBb	$8.7^{\circ} \pm 0.8$ (13, 18)	$28^{\circ} \pm 2$ (2)	3	$21^{\circ}$	0.80	39
UGC 3900	SBb	$7.1^{\circ} \pm 0.2$ (13, 25)	$10^{\circ} \pm 3$ (2)	1	$26^{\circ}$	0.78	154
UGC 3936	SBbc	$7.6^{\circ} \pm 0.3$ (10, 27)	$9^{\circ} \pm 4$ (2)	4	$24^{\circ}$	0.81	76
UGC 4643	SAbc	$4.1^{\circ} \pm 0.6$ (9, 30)	$31^{\circ} \pm 2$ (3)	4	$48^{\circ}$	0.72	214
UGC 5434	SABb	$8.7^{\circ} \pm 0.5$ (8, 15)	$37^{\circ} \pm 5$ (2)	2	$31^{\circ}$	0.93	130
UGC 6166	Sbc	$10.6^{\circ} \pm 1.0$ (10, 22)	$6^{\circ} \pm 1$ (1)	2	$20^{\circ}$	0.89	45
UGC 6332	SBa	$7.6^{\circ} \pm 0.2$ (14, 27)	$24^{\circ} \pm 4$ (2)	4	$37^{\circ}$	0.67	51
UGC 6958	SABbc	$7.4^{\circ} \pm 0.4$ (8, 16)	$38^{\circ} \pm 2$ (1)	2	$72^{\circ}$	0.89	44
UGC 8939	SABb	$5.3^{\circ} \pm 0.6$ (7, 15)	$10^{\circ} \pm 2$ (2)	4	$15^{\circ}$	0.72	128
UGC 11524	SAc	$7.5^{\circ} \pm 0.5$ (8, 27)	$20^{\circ} \pm 4$ (2)	2	$63^{\circ}$	0.82	152

**Table 2.** Relative Strengths of the Fourier modes

Galaxy Name	Fourier Mode			
	m=1	m=2	m=3	m=4
ESO 555 -G 013	1.9	2.5	4.2	1.8
IC 357	1.7	0.6	1.0	1.9
IC 568	1.0	2.1	0.7	1.0
IC 742	4.8	0.3	0.8	2.4
IC 1196	2.6	0.3	1.6	1.1
IC 1764	1.9	2.2	0.9	2.0
IC 1809	1.0	0.7	1.3	2.1
IC 2363	0.1	1.2	2.6	6.4
IC 3692	1.3	1.0	1.0	0.9
NGC 1219	2.1	0.4	1.5	2.8
NGC 2416	1.9	0.9	0.3	0.6
NGC 2503	1.2	1.8	0.3	2.2
NGC 2529	1.5	0.6	1.4	1.3
NGC 2628	1.0	3.0	0.5	0.9
NGC 3512	2.2	1.1	1.6	1.1
NGC 5478	1.6	1.2	1.5	1.1
NGC 5737	1.7	0.7	0.7	2.4
NGC 6347	0.9	2.3	0.2	3.8
NGC 6379	3.1	0.9	0.3	0.9
NGC 6574	3.6	0.4	1.3	3.5
UGC 850	0.2	4.1	1.5	2.2
UGC 1478	5.7	2.8	1.5	1.2
UGC 1546	1.8	7.8	0.4	1.3
UGC 2303	1.4	1.2	2.9	1.9
UGC 2585	2.1	4.7	1.3	0.4
UGC 2705	1.1	2.2	3.7	0.9
UGC 2862	0.9	1.0	1.1	0.9
UGC 3053	2.1	1.3	1.8	0.2
UGC 3091	2.8	1.6	2.2	2.3
UGC 3171	1.9	0.7	0.7	0.8
UGC 3233	2.6	3.0	0.7	1.8
UGC 3296	1.1	4.8	2.6	1.0
UGC 3578	1.0	1.2	0.9	0.9
UGC 3707	7.0	1.5	1.4	0.2
UGC 3806	1.5	0.7	0.9	1.5
UGC 3839	1.0	1.1	1.9	1.6
UGC 3900	3.5	0.9	0.3	0.5
UGC 3936	1.1	0.7	1.6	2.2
UGC 4643	0.2	1.9	0.7	1.9
UGC 5434	0.4	3.7	0.7	3.4
UGC 6166	0.5	1.1	0.1	0.8
UGC 6332	2.2	0.6	0.3	4.0
UGC 6958	0.9	8.7	1.2	5.9
UGC 8939	1.3	0.9	0.9	2.0
UGC 11524	1.3	1.8	1.6	0.8

**Table 3.** Comparison of overall K-band arm strengths with overall B-band arm strengths. Arm strengths are measured in terms of EA in degrees.

Galaxy	Overall Arm strength	
	K-band	B-band
NGC 5478	37.0±1.9	19.5±2.0
UGC 6958	38.0±2.4	15.4±1.3
UGC 8939	10.4±2.1	23.4±0.7

**Table 4.** Comparison of arm properties between B-band and K-band images measured for the strongest arm in the galaxies.

Galaxy	B-band		K-band	
	Pitch Angle	Azimuthal angle at start of arm	Pitch Angle	Azimuthal angle at start of arm
NGC 5478	10.9 $\pm$ 1.3	224°	9.9 $\pm$ 1.1	219°
UGC 6958	9.3 $\pm$ 1.5	347°	7.4 $\pm$ 1.4	342°
UGC 8939	5.5 $\pm$ 0.6	363°	5.1 $\pm$ 0.6	355°

Figure 1: Arm profiles in terms of arm equivalent angle versus radius.

Figure 2: Arm cross-sections (top), symmetric components (central) and antisymmetric components (lower). Leading edges (i.e. the convex sides) of arms are plotted on the right. A  $540^\circ$  cut of IC 1809 is also shown (bottom).

Galaxies with companions within 6 galaxy diameters shaded in black; (b) Galaxies with bars stronger than the average overall bar strength shaded in black.

Figure 4: Pitch angle versus fraction of K-band light in the disk.

Figure 5: Pitch angle versus Hubble type. The line represents the correlation predicted by Roberts et al. (1975).

Figure 6: The galaxy NGC 2503 in polar coordinates.  $100 \ln(r)$  is plotted in the x direction where  $r$  is measured in pixels.  $\theta$  is plotted in the y direction in units of degrees, so the plot represents a turn and a half around the galaxy. The arms appear straight (with a constant gradient) in this plot and their pitch angles can be measured directly from their gradients. NGC 2503 demonstrates that pitch angle is not the same even for arms within the same galaxy.

Figure 7: Arm strength in the inner part of the disk versus bar strength for all the barred galaxies in the sample. Bar strength and arm strength are both measured in terms of EA in degrees.

Figure 8: Greyscale unsubtracted and difference images of the galaxy UGC 3900 showing that its arms start ahead of the end of its bar and that its bulge is offset from the centre of the disk. The axes are labelled in units of pixels, where 1 pixel = 0.286 arcsec.

Figure 9: Arm strengths in terms of EA; galaxies with near neighbours are shaded in black.

Figure 10: Distribution of the azimuthal angles subtended by arms; galaxies with near neighbours are shaded in black.

Figure 11: Azimuthal angle subtended by arms (in degrees) against bulge-to-disk ratio.

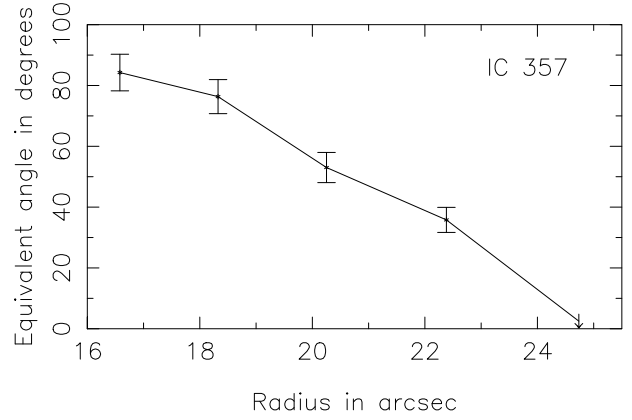
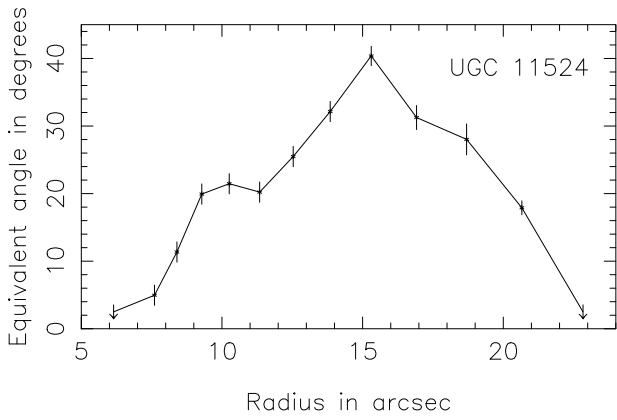
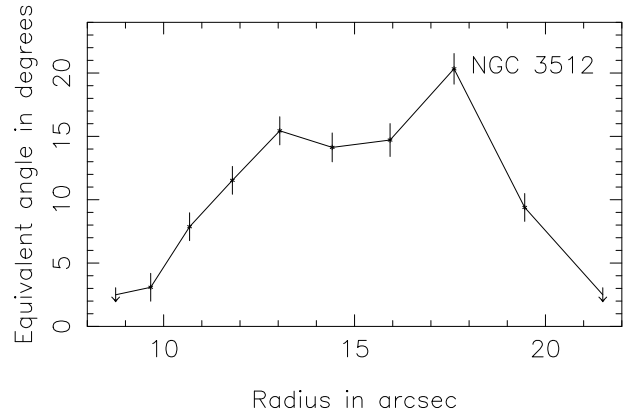
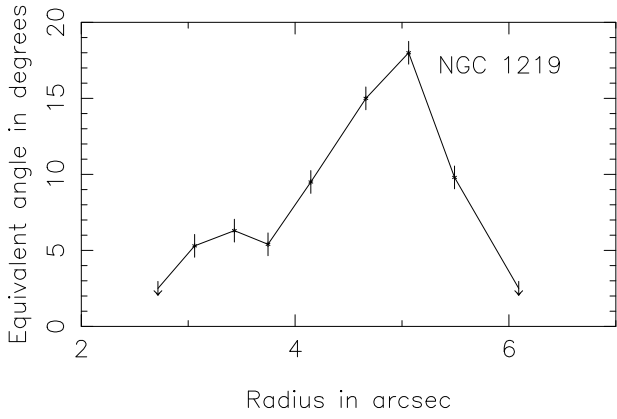
Figure 12: Arm strength (in terms of EA in degrees) versus disk central surface brightness (K-mag per square arcsec).

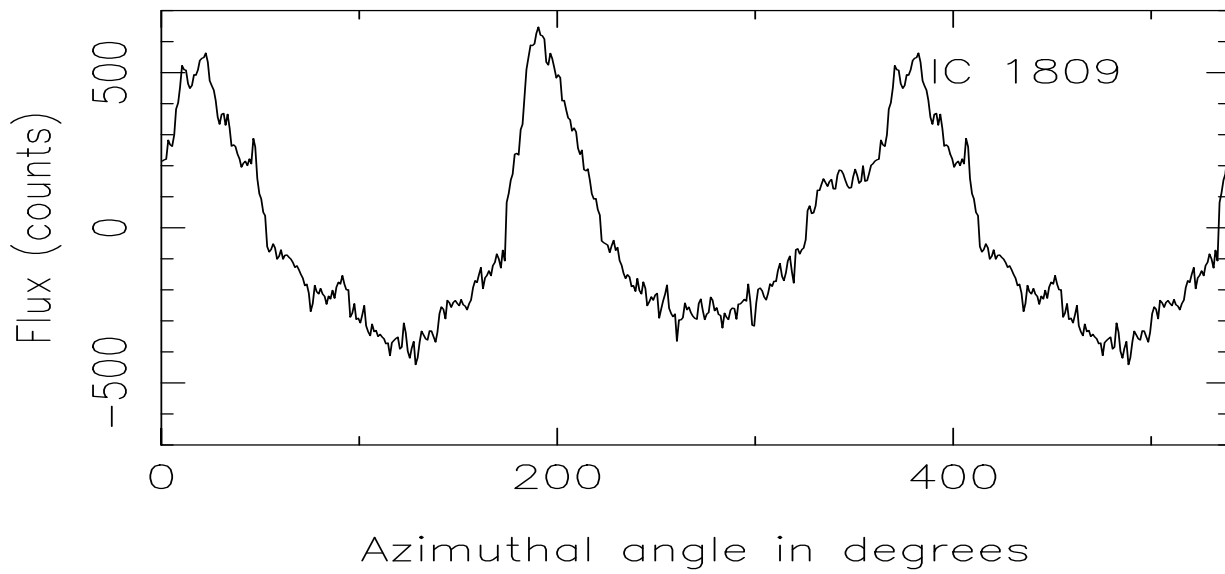
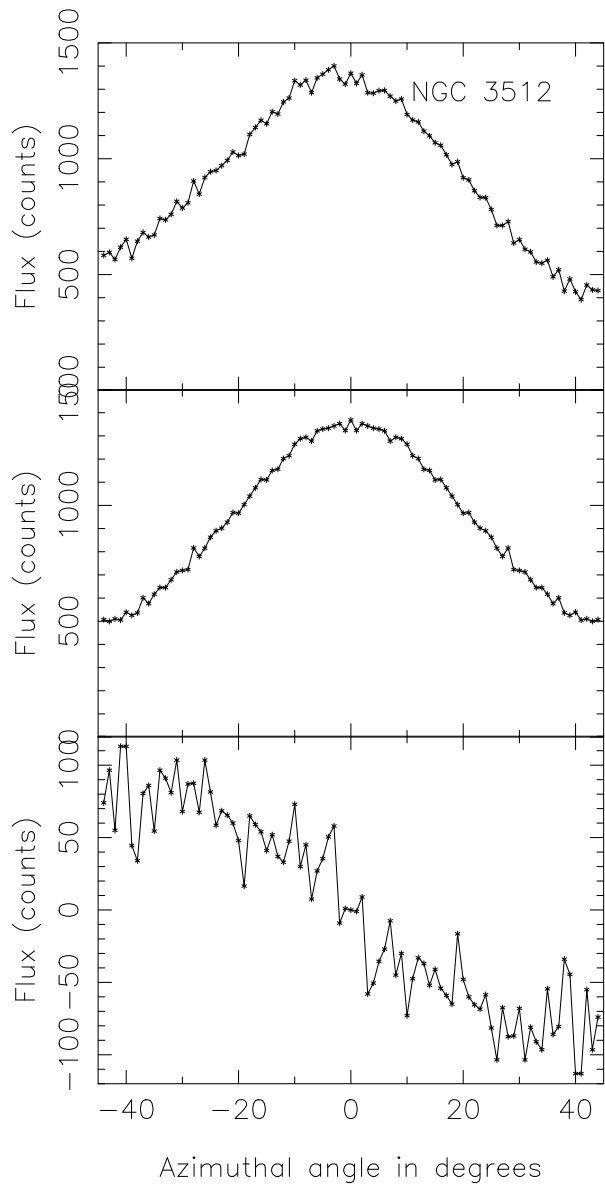
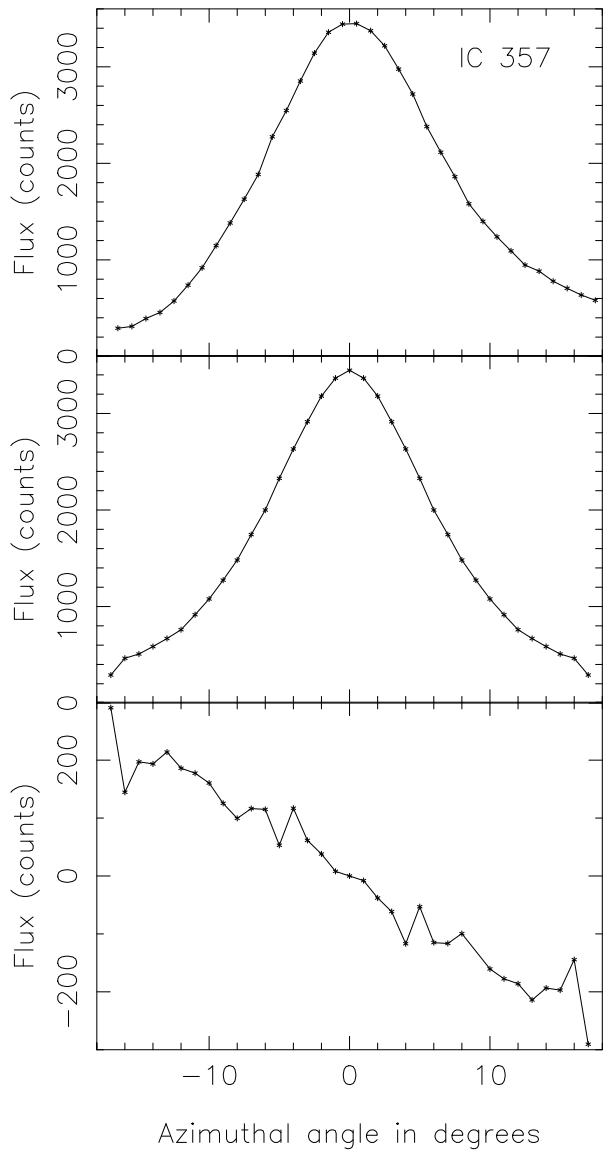
Figure 13: Far-infrared bolometric luminosity normalised to K-band magnitude versus arm contrast. The point represented by a hollow circle is IC 568, which we believe has a starburst nucleus that probably dominates its FIR luminosity. The line is an error weighted regression, ignoring IC 568.

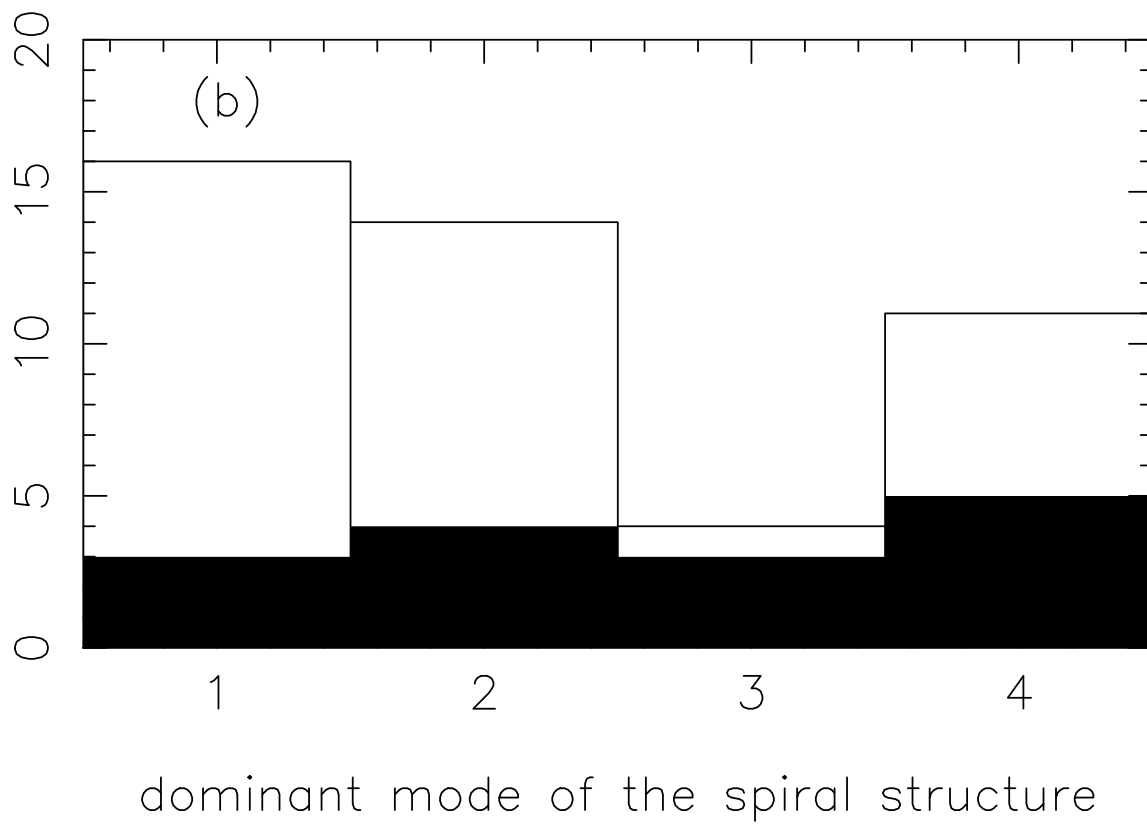
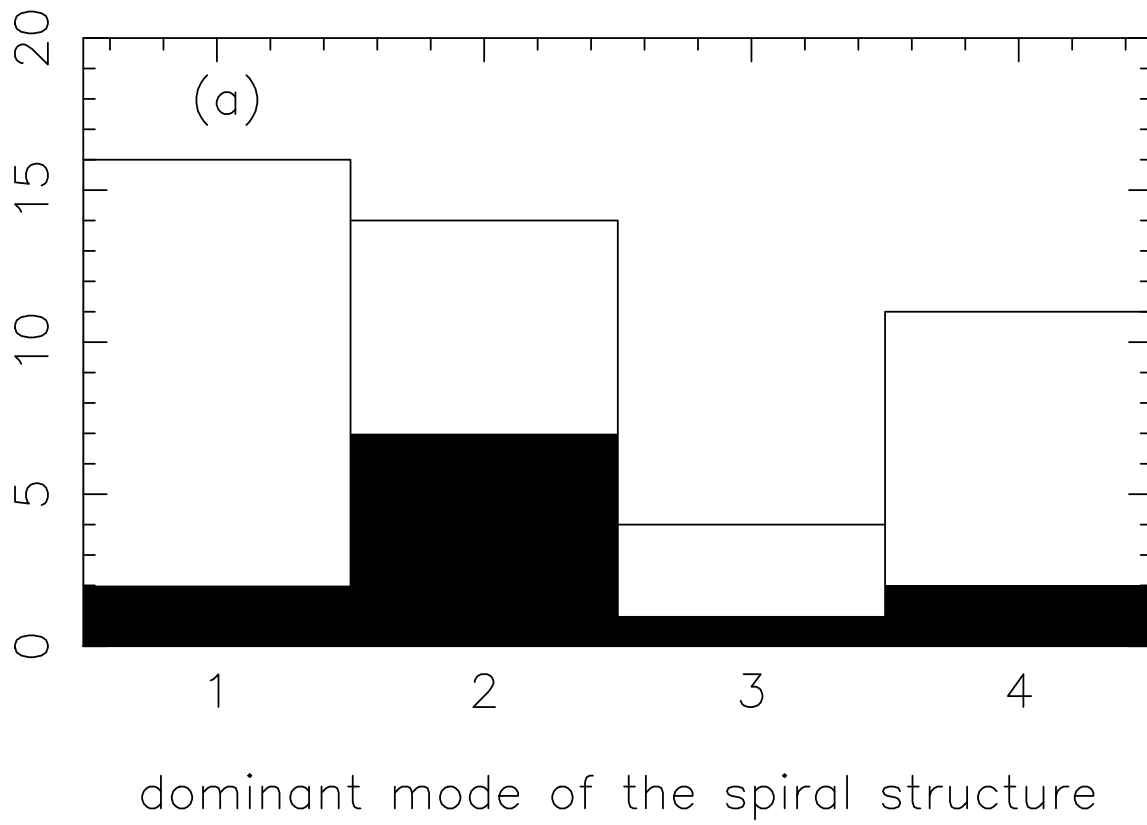
Figure 14: Radial dependence of the difference in azimuthal angle between B-band and K-band arms.

Figure 15: Comparison of K-band arm cross-sectional profiles with B-band cross-sectional profiles. K-band data are represented by circles and B-band data are represented by squares.

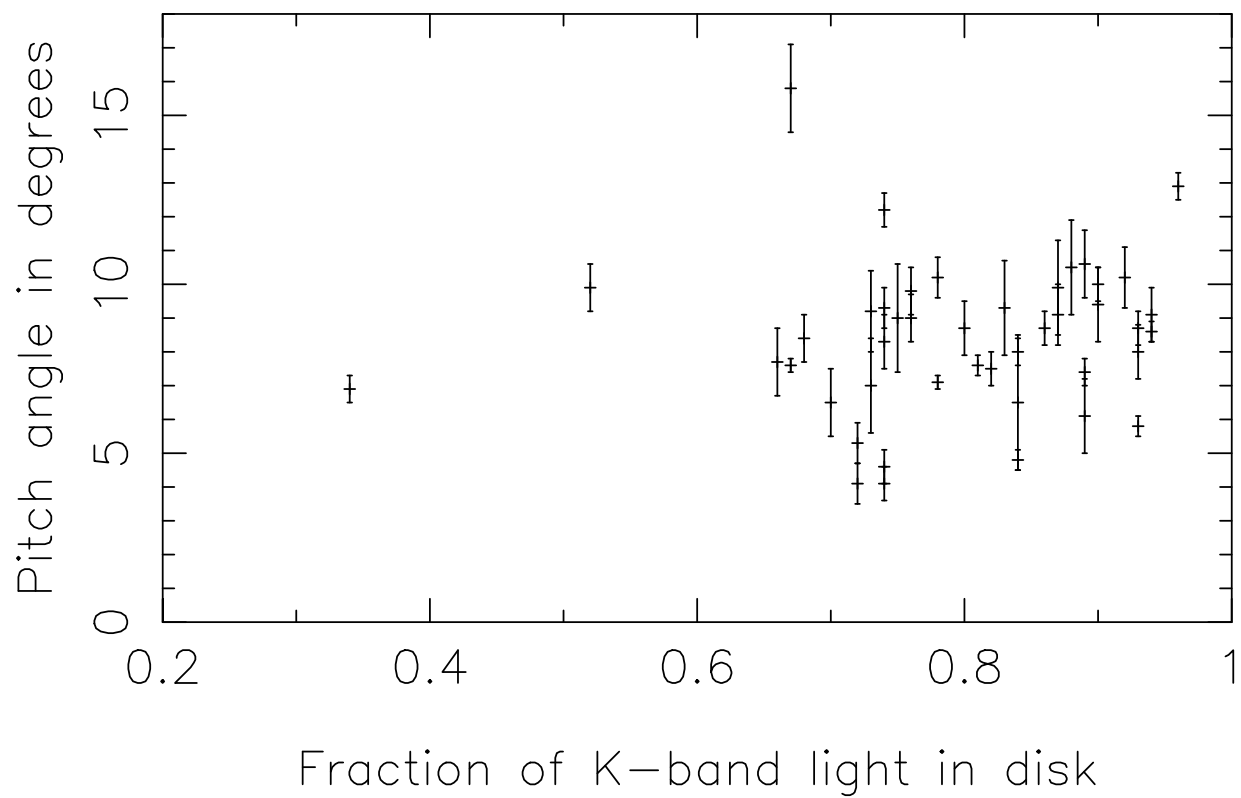
Figure 3: The occurrence of the strongest Fourier modes found in the disks of the entire sample compared with (a)

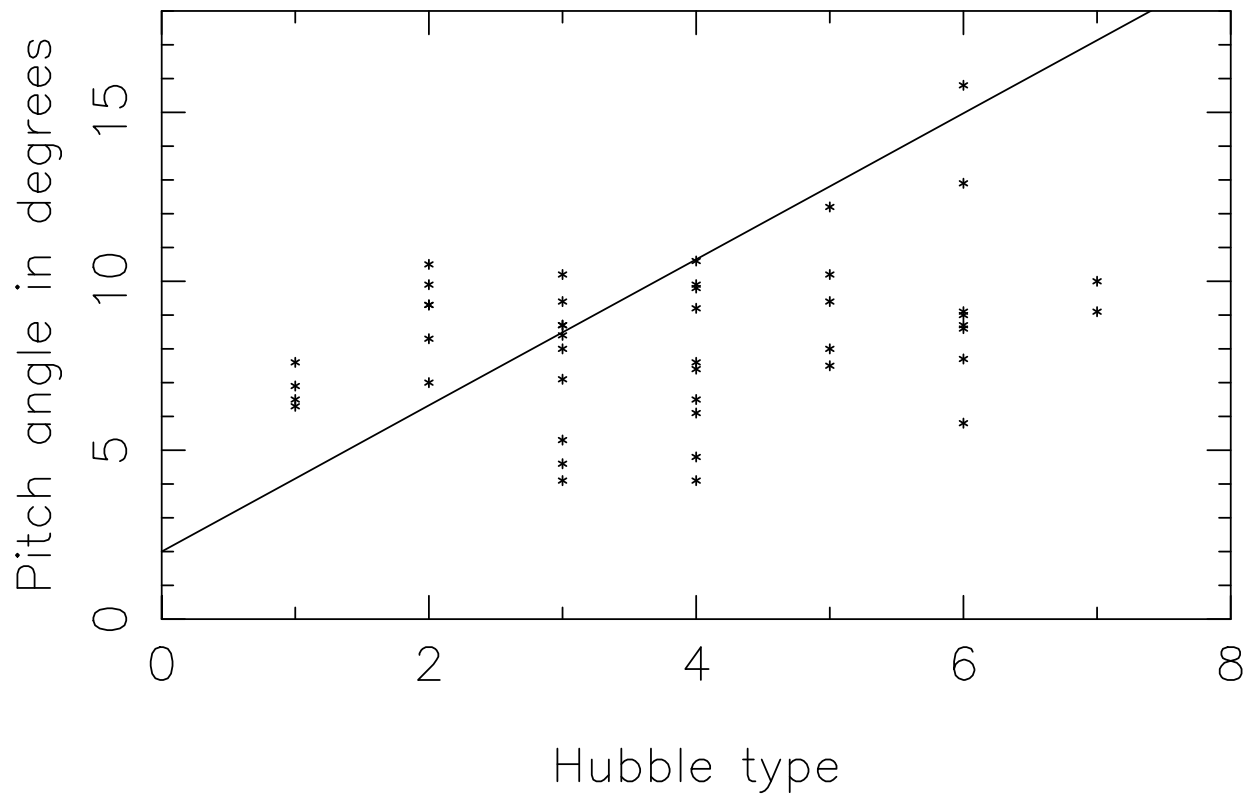


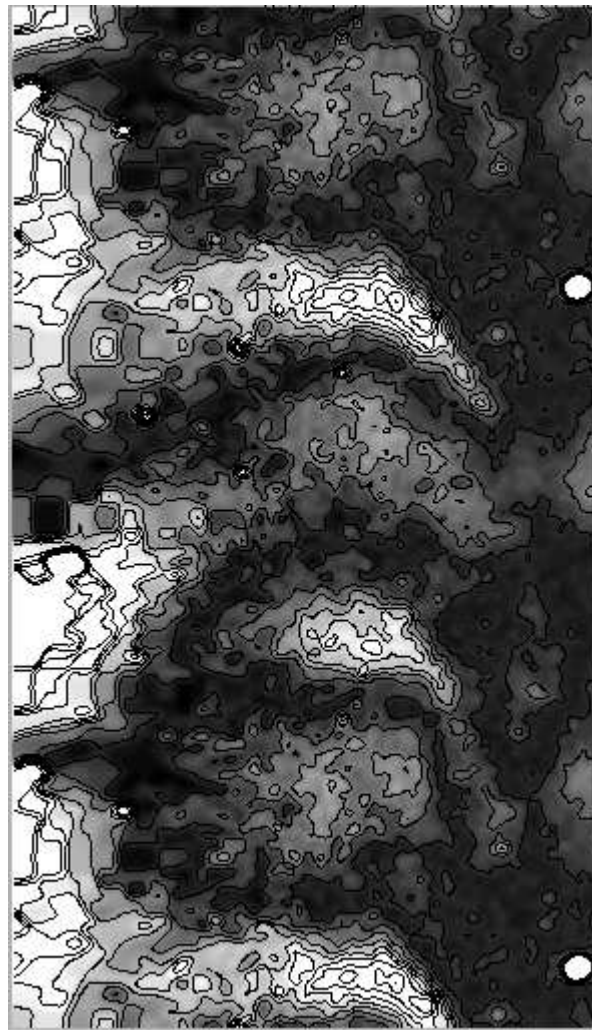


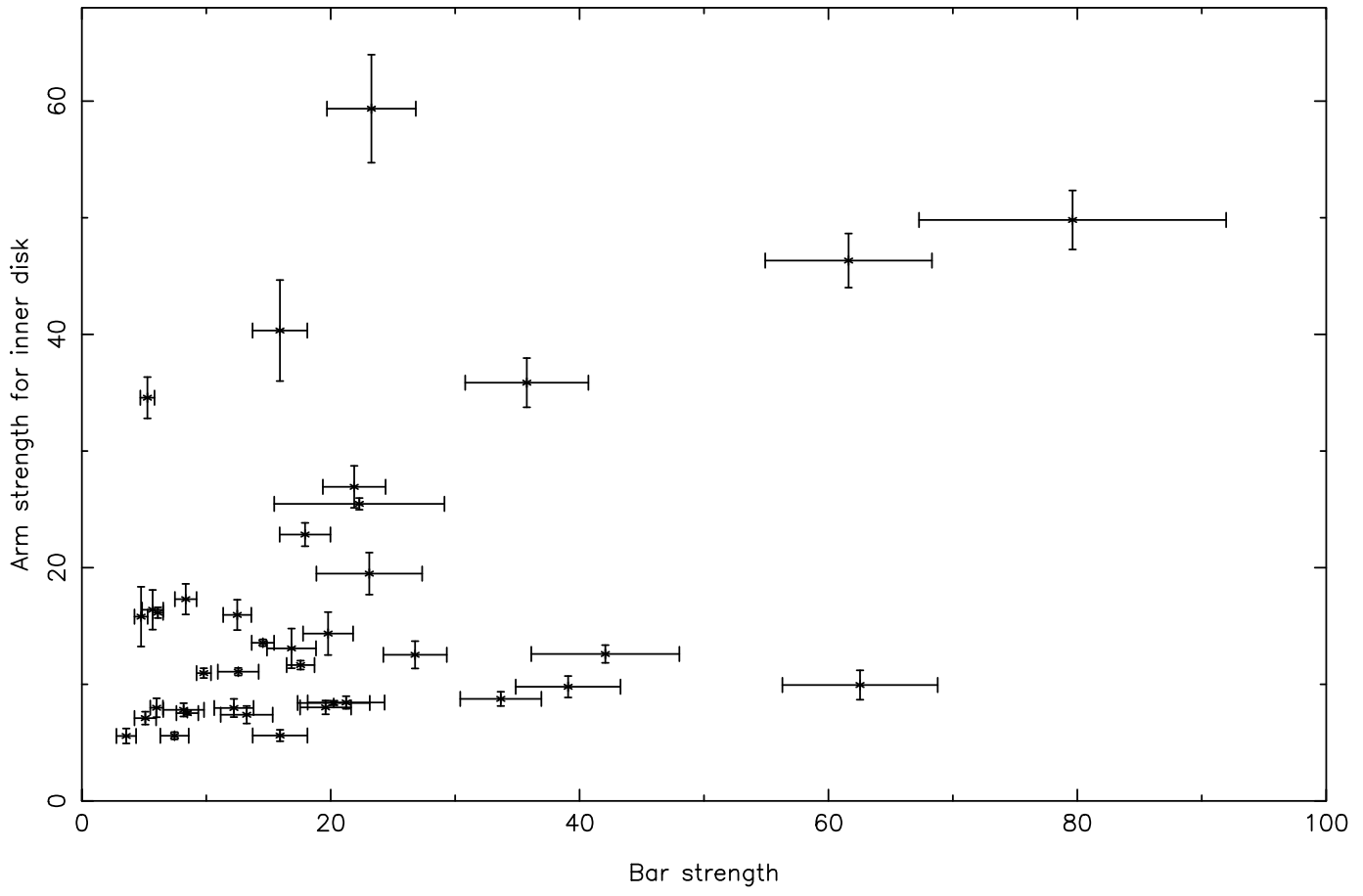


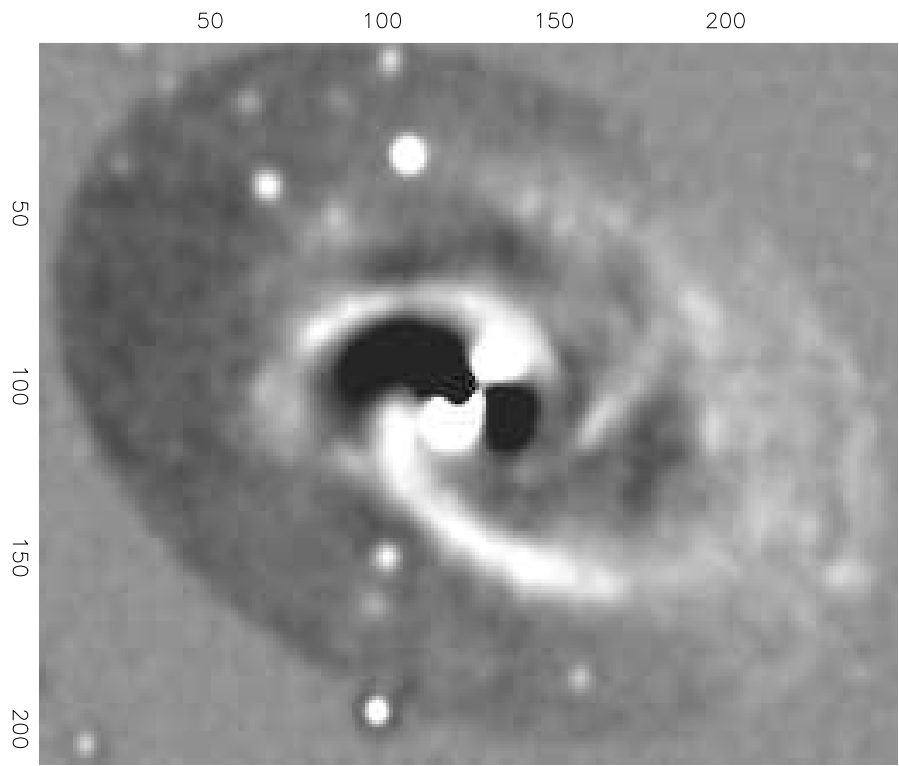
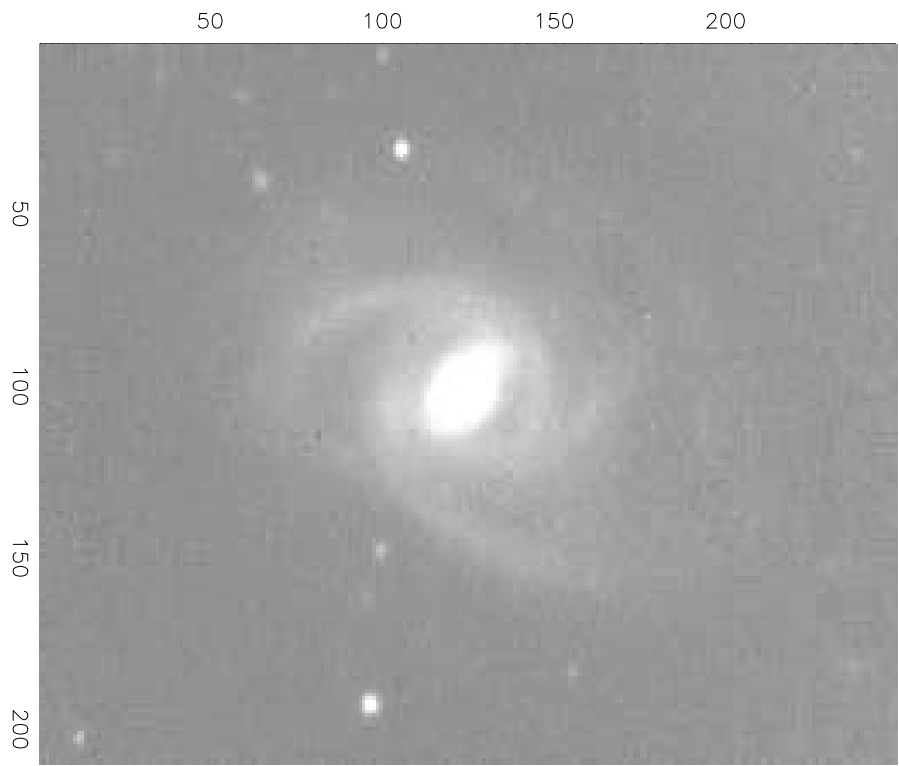


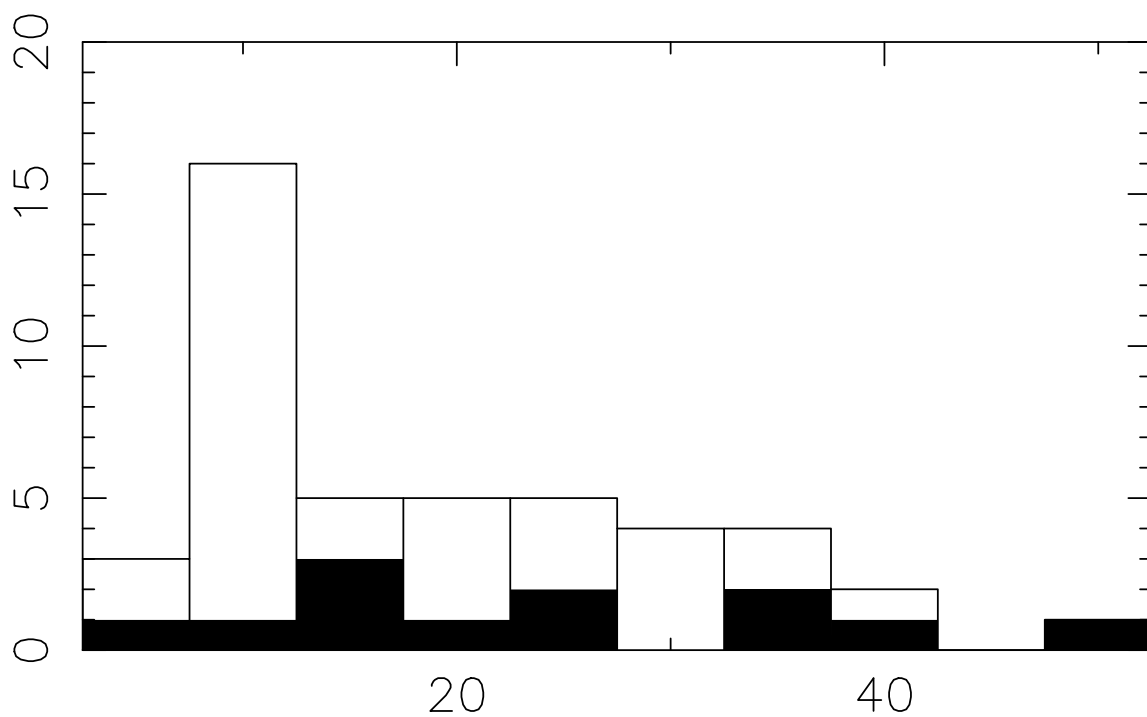




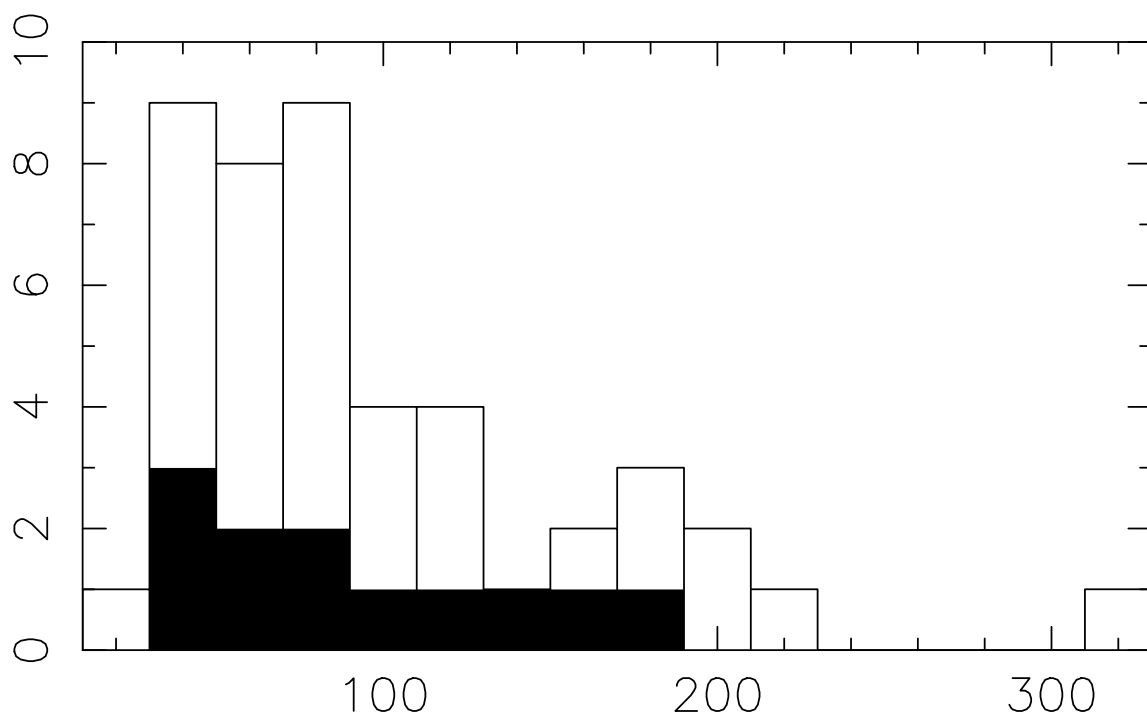






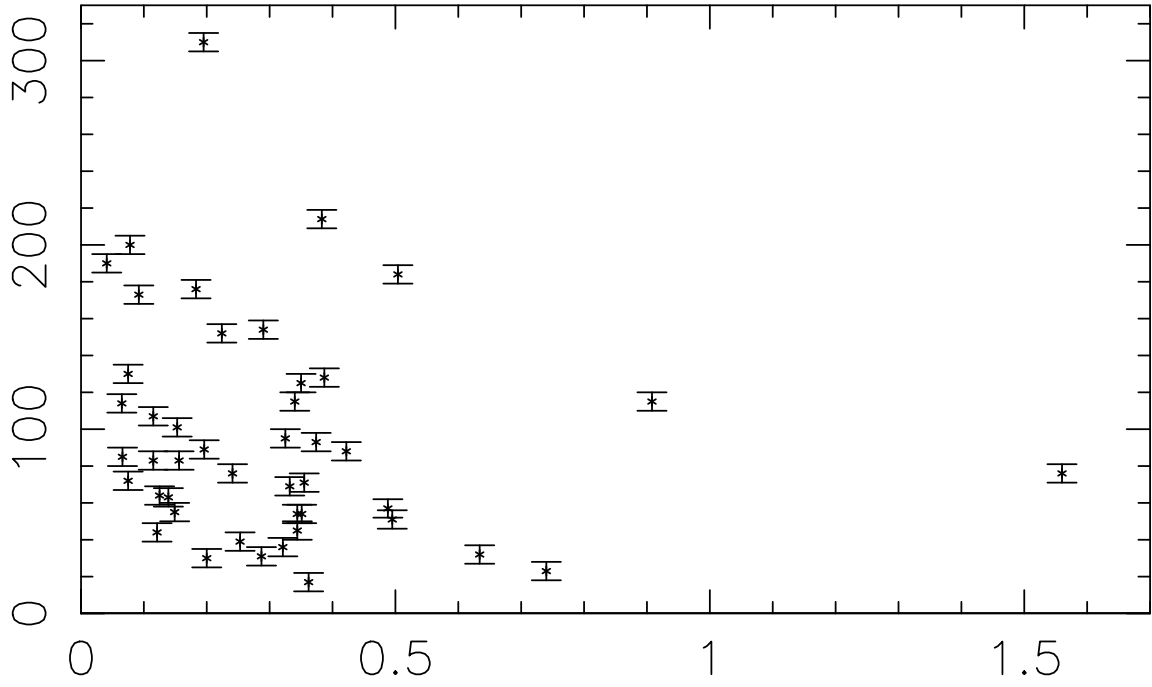


Arm strength in terms of overall EA



Azimuthal angle subtended by arms

Azimuthal angle subtended by arm



Bulge-to-disk ratio



